

Identifying mass composition of ultra-high-energy cosmic rays using deep learning

O. Kalashev,^{a,b} I. Kharuk,^{a,b} M. Kuznetsov,^{a,c} G. Rubtsov,^a T. Sako,^d Y. Tsunesada,^{e,f} Ya. Zhezher,^{a,d}

^a*Institute for Nuclear Research of the Russian Academy of Sciences,
60th October Anniversary Prospect, 7a, Moscow, 117312, Russia*

^b*Moscow Institute of Physics and Technology,
Institutsky lane 9, Dolgoprudny, Moscow region, 141700, Russia*

^c*Service de Physique Théorique, Université Libre de Bruxelles,
Boulevard du Triomphe CP225, 1050 Brussels, Belgium*

^d*Institute for Cosmic Ray Research (ICRR), University of Tokyo
5-1-5 Kashiwanoha, Kashiwa-shi, Chiba 277-8582, Japan*

^e*Graduate School of Science, Osaka City University,
Osaka, Osaka, 558-8585, Japan*

^f*Nambu Yoichiro Institute of Theoretical and Experimental Physics, Osaka City University,
Osaka, Osaka, 558-8585, Japan*

E-mail: ivan.kharuk@phystech.edu

ABSTRACT: We introduce a novel method for identifying the mass composition of ultra-high-energy cosmic rays using deep learning. The key idea of the method is to use a chain of two neural networks. The first network predicts the type of a primary particle for individual events, while the second infers the mass composition of an ensemble of events. We apply this method to the Monte-Carlo data for the Telescope Array Surface Detectors readings, on which it yields an unprecedented low error of 7% for 4-component approximation. The statistical error is shown to be inferior to the systematic one related to the choice of the hadronic interaction model used for simulations.

Contents

1	Introduction	1
2	Deep learning for reconstructing mass composition	3
2.1	Data	3
2.2	Event-by-event analysis	3
2.3	Identifying mass composition	7
2.4	Model dependence	9
3	Conclusion	11
A	Regression approach	11
B	Composition-sensitive parameters and cuts	12

1 Introduction

Ultra-high-energy cosmic rays (UHECR) are particles with energies greater than 10^{18} eV reaching Earth from the cosmos. Understanding their origin is one of the most important unresolved problems in modern astrophysics. The information on nuclear types of cosmic rays primary particles (proton, helium, etc.) is crucial for achieving progress in this task. However, identifying UHECRs mass composition, i.e. the types of primary particles and their relative fractions in the spectrum, remains a challenging task.

It is known that the UHECR flux consists mostly of protons and nuclei [1] with only small admixtures of photons [2, 3] and neutrinos [4, 5] allowed. UHECR mass composition is the key observable for distinguishing between various models of cosmic-ray production [6, 7], as well as understanding the physical nature [8–10] of their energy spectrum cutoff [11–13]. Knowing the mass composition is also important for the prospective cosmic ray astronomy. Namely, for proton-dominated composition UHECR arrival direction is expected to trace their sources. On the other hand, for nuclei-dominated composition this would not be the case due to large deflections in the galactic magnetic fields [14].

The most accurate studies of UHECR mass composition are performed by measuring the longitudinal profiles of extended air showers by the fluorescence detectors [11, 15–18]. However, fluorescence detectors can operate only at moonless nights and under good weather conditions, which strongly limits the number of observable events per year.

An alternative approach is to use the readings of the surface detectors, which can collect data during almost the whole year. The trade-off is that surface detectors provide less informative data as compared to the one obtained with fluorescence detectors. Hence,

to get a competitive accuracy, one needs to employ machine learning techniques. For example, this approach was undertaken in recent studies [19, 20].¹

The aim of the present paper is to develop further machine learning techniques used for analyzing surface detectors data. We start by highlighting the two key aspects of the underlying problem.

The first one is related to the stochastic nature of an extensive air shower. Namely, extensive air showers are initiated by high-energy cosmic rays, which, upon entering Earth's atmosphere, interact with the nuclei of atoms. This results in an avalanche-like production of particles, whose footprints are measured by detectors on the ground level. The position of interaction points, as well as particles' properties after the interaction, follow some probability distributions. This makes the evolution of an air shower stochastic in nature and results in the variability of the footprints. In practice, the situation is complicated further by the presence of detectors triggered by occasional muons, irregular detector grid, saturated and offline detectors. As a consequence, different primary particles may yield similar footprints, which lowers the efficiency of standard machine learning techniques.

The second aspect is that there exist several hadronic interaction models used for simulating air shower evolution. Different models yield considerably different air shower properties at the ground level. Moreover, some experiments observe the excess of the observed muons signal as compared to the simulations [23–27], while others do not [28–31] (see [32] for a review). This imposes certain limitations on the use of hadronic interaction models for analyzing the actual experiment's data.

In the paper we develop a method, which is less affected by the first of the mentioned problems. The progress is achieved by introducing a chain of two neural networks for analyzing the data. The first network analyzes individual events and predicts the corresponding primary particle. The second network analyzes ensembles of events and reconstructs the mass composition based on the inference of the first network. We apply this method to the Monte-Carlo set with four cosmic ray primaries (proton, helium, nitrogen, and iron) for the surface detector readings of the Telescope Array experiment [33]. For a given hadronic model our approach yields unprecedentedly low error — the fractions of primary particles in an ensemble of events are reconstructed with an error less than 7%.

The developed approach allows one to obtain accurate predictions for an ensemble of events despite high variability of data for individual events. This makes it applicable for a wide range of experiments with similar specifics of the data.

The paper is organized as follows. In section 2.1 we briefly describe the Telescope Array experiment and the Monte-Carlo set we are using. Section 2.2 is devoted to the discussion of the neural network used for analyzing individual events. In section 2.3 we introduce the second neural network, which is used for estimating UHECR mass composition. Model dependence of the predictions with respect to changing the hadronic interaction model used for simulations is studied in section 2.4. Finally, section 3 concludes the paper.

¹We would also like to mention that it is possible to infer UHECR mass composition based on the detailed UHECR flux modeling and their energy spectrum [21] or arrival directions [22].

2 Deep learning for reconstructing mass composition

2.1 Data

Telescope Array Observatory is located in Utah, USA, and is the largest cosmic ray detector in the Northern Hemisphere aimed at studying UHECR. The Telescope Array Surface Detector includes 507 scintillation surface detectors placed on a square grid, with a 1.2 km spacing, covering an area of approximately 700 km². Each detector has two layers of 1.2 cm thick plastic scintillator, which is sensitive to both electromagnetic and muon components of the air shower [33]. Each layer measures time-resolved signal with 20 ns time bin size. The signal is converted to conventional units called “minimal ionization particles” (MIP) using the calibration information which is recorded every 10 minutes for each detector. The same calibration information is used in Monte-Carlo simulations as well.

An *event* is recorded when the trigger condition is satisfied, see [33] for details on the triggering system. For each event, the corresponding record includes *i*) time series of the signal from each of the activated detectors and *ii*) starting time of the recordings. Further, the parameters of the air shower, such as Linsley front curvature and energy of the primary particle, are estimated using the reconstruction procedure [13] (see Appendix B for details).

Experimental data is modeled via Monte-Carlo simulation using CORSIKA software [34] with protons, helium, nitrogen, and iron as primary cosmic ray particles. Energy spectrum of the simulated events coincides with the one measured in the HiRes experiment [11], and the number of simulated showers is the same for all primaries. The procedure accounts for offline detectors, saturated detectors and muons from randomly coincident low-energy showers.

We are using data simulated with QGSJET II-03 hadronic model [35] passing the following quality cuts: *i*) energy of a primary particle estimated with the standard TA Surface Detector reconstruction procedure is larger than 1 EeV, *ii*) reconstructed zenith angle of a primary particle is below 45°, *iii*) the number of triggered detectors is 7 or more, *iv*) small error of the reconstructed parameters (see Appendix B for details). In total, for all primaries we have 481 172 Monte-Carlo events satisfying these conditions.

2.2 Event-by-event analysis

In previous work [36] the reconstructed parameters, such as Linsley front curvature and area-over-peak, were used to predict the mass of the primary particles using Boosted Decision Trees. As an improvement to this approach, we switch to using neural networks instead of Boosted Decision Trees for this task. This allows us to incorporate more data into the analysis (such as raw readings of the detectors) and employ advanced machine learning techniques. The benefits of using neural networks in similar tasks were demonstrated, for example, in [37], where they are used for reconstructing cosmic rays arrival directions.

The first step of our method consists of classifying individual events using a neural network. In what follows we refer to this network as *the classifier*. Its architecture, depicted in figure 1, can be splitted into four blocks, each of which is responsible for processing

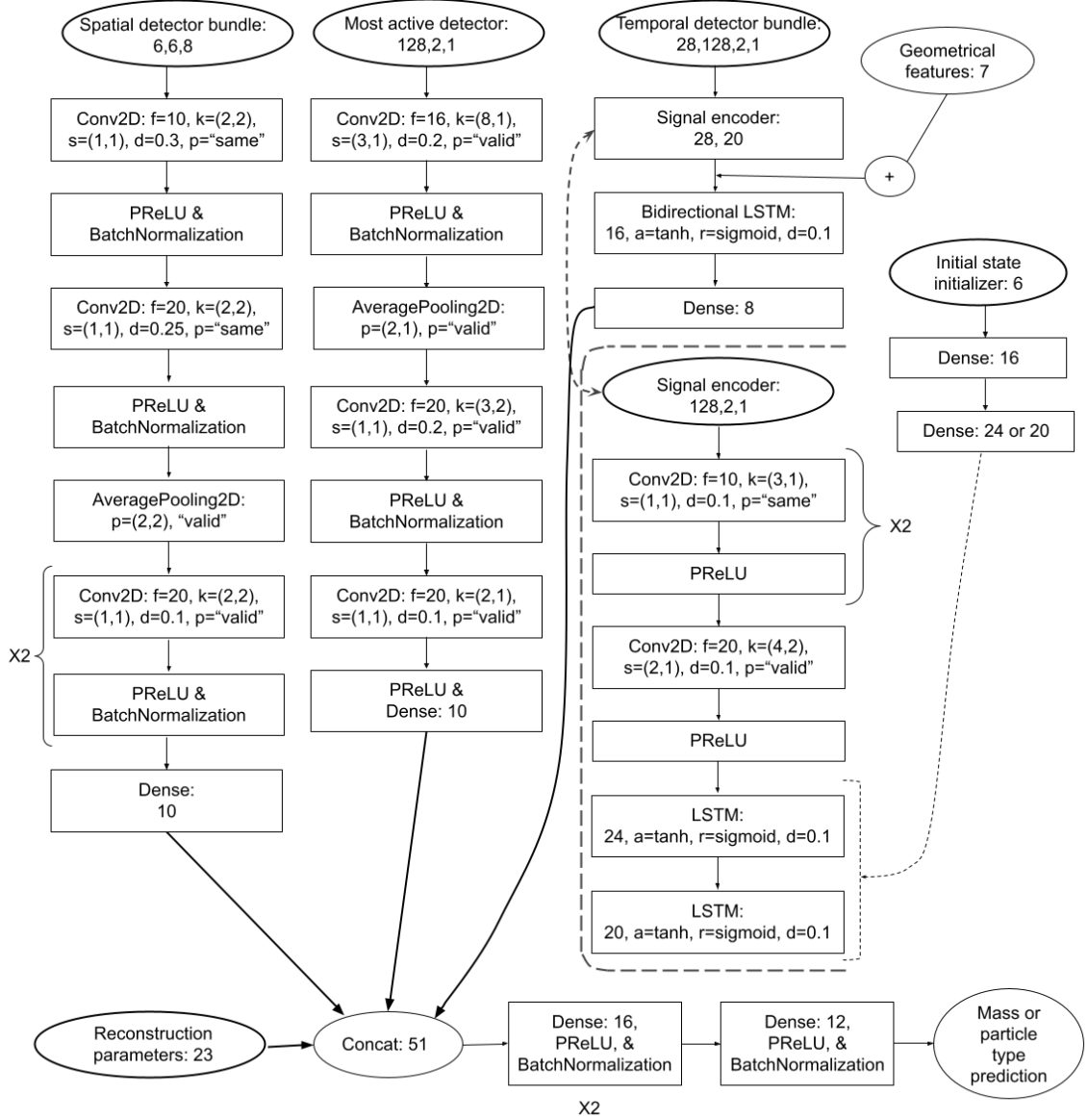


Figure 1. Architecture of the neural network. The flow of the data is shown by arrows. Layers names are given according to TensorFlow API. Abbreviations: “f” — number of filters, “k” — kernel size, “s” — strides, “d” — dropout rate, “p” — pooling size or padding regime, “a” — activation function, “r” — recurrent activation function, number after colon — input shape or number of units.

certain kind of data gathered from an event. Below we describe the blocks one by one, highlighting their general features.

1. *Spatial detectors bundle.* For each event we construct a six by six grid of detectors centered on the averaged position of the triggered detectors. In each “detector cell” we store eight parameters:

1-2) x and y coordinates of the detector relative to the reconstructed position of the air

shower core,

- 3) the position of the detector with respect to the conventional zero-ground level,
- 4) detector's integral signal (sum of detector's readings),
- 5) reconstructed time of the plane front arrival to the detector,
- 6) time difference between the earliest timestamp of the recorded signal and the moment of the plane front arrival at the detector,
- 7) whether detector was triggered,
- 8) whether detector's readings were significantly longer than 128 bins (2.56 ms).

Altogether this can be treated as a six by six “pixel image” with 8 channels (instead of standard RGB). Convolution neural networks are known to be well-suited for analyzing such kind of data. Accordingly, we pass the above-mentioned data through a number of convolution layers to obtain spatial (geometrical) features of an event.

2. *Signal from the detector with the largest integral signal.* For a given detector the signal may last as long as 500 time bins. As in average the length of a signal is much shorter, we cut all signals to 128 bins to unify detectors' readings. It was verified that increasing this number does not improve neural network performance. A typical signal from one of the detector's layers is illustrated in figure 2. Notice that the peaks in the signal are rather sharp. To soften them, we employ the signal conversion to the logarithmic scale by taking $\ln(1 + \text{signal})$ as the input for the neural network.

Detector's readings can be thought of as a one-dimensional image with two channels (one channel per detector layer). Correspondingly, we pass the signal through a series of convolution layers to obtain the features of the largest signal.²

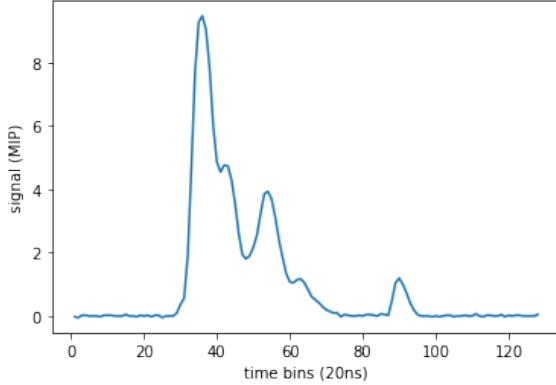


Figure 2. An example of detector's reading from one of the layers.

3. *Temporal detector bundle.* To get temporal characteristics of an event, we collect all triggered detectors and order them in a one-dimensional chain according to the time of

²One can analyze the signal by recurrent layers. However, we found no difference in the resulting precision, while convolutions are computationally much faster.

the plane front arrival. On Monte-Carlo data the number of the triggered detectors varies from 7 to 41 from event to event. Our practice showed that the chain can be safely cut down to 28 cells without losing neural network's performance, . In each cell we put the time series of the corresponding detector readings (reduced to 128 time bins as described above).

To process the data, we first analyze the signal in each cell of the chain by a *signal encoder*. As the first step, the encoder passes the time series of the signal through several convolution layers. Further, the resulting data is passed through recurrent cells, which are known to be well-suited for analyzing time-ordered information.³ This procedure yields signal encodings for each of the detectors.

Similarly to [38], we use a small fully connected neural network for setting the initial state of the recurrent cells analyzing the signal in the signal encoder. The input data for this network includes 6 parameters: x, y, and z coordinates of the detector, reconstructed time of the plane front arrival, time difference between starting point of detectors' recordings and the time of plane front arrival, and reconstructed zenith angle of the primary particle.

As the next step, the obtained encodings are concatenated with geometrical characteristics of the corresponding detectors (parameters 1–6 and 8 used in spatial detector bundle). Together they represent air shower and detector properties at detector's location, ordered according to the time of the plane front arrival. Finally, the 28 cells with thus obtained information are analyzed by recurrent layers to obtain temporal features of an event.

4. Combination layer. At the final layer we concatenate all of the obtained features and supplement them with useful reconstruction parameters. The latter include zenith angle, normalization of the shower lateral distribution profile S_{800} , and composition-sensitive parameters (see Appendix B for the full list of parameters). Together they are passed through several fully-connected layers to make the final prediction. The latter can be either the mass of the primary particle or its type.

The most important block in the neural network is the temporal detector bundle as it utilizes all available information on an event. Reconstruction parameters carry high-level information, like air shower's front curvature, and thus are expected to be the next by relevance. Spatial detector bundle yields geometrical features of an event, placing it third by relevance. Finally, the block analyzing the signal from the most active detector is of least importance as it utilizes the least amount of information. We confirm this ranking of the blocks by providing their individual precisions later in this section.

The classifier is implemented in TensorFlow [39] and optimized using Keras-Tuner [40] on 1/3 of the training and validation data sets. The full architecture of the model, including layer specifics, is presented in figure 1. In total, the neural network has $\sim 35\,000$ trainable parameters. For training the network we used Adam optimizer [41] with *amsgrad* modification [42].

One can approach the task of identifying the mass composition of UHECR as a classification or regression problem, i.e. predict the type of primary particle or its mass. Below

³Unlike the analyzes of a signal from the detector with largest signal, the use of recurrent cells yields an improvement in the performance.

	temporal detector bundle	reconstruction parameters	spatial detector bundle	most active detector
accuracy	39.5%	33.8%	32.9%	31.0%

Table 1. Accuracies of different blocks of the classifier.

we focus on the former approach (classification) and comment on the alternative one in Appendix A.

We found it beneficial to train the classifier in two steps. First, the network is trained on all available events. Then, at the second stage, its training is continued only on the events in a certain energy bin. Such procedure allows the network first to capture general features of the events, and then fine-tune itself for specific energies.

To illustrate the method, we further consider the network trained for the events in the $10^{18.75} - 10^{19.00}$ eV energy bin during the second stage of training. The corresponding Monte-Carlo set consists of 103 752 events, 80% of which were used as the training set and the rest as the validation (test) set. The results for other energy bins are similar and are presented in the table at the end of next section.

On an event-by-event basis, the accuracy of our best-trained classifier was 40.2%. This is far from being an ideal precision, yet much better than random guessing (25%) and the accuracy of boosted decision trees used earlier for this problem ($\sim 31\%$). We have also established the contribution of each of the neural network's blocks to the final accuracy by training neural networks consisting of only one of the blocks. The results are presented in table 1, and they confirm our expectations on the importance of the blocks.

2.3 Identifying mass composition

A naive method for obtaining the mass spectrum for an ensemble of events would be to average the predictions of the classifier over events. However, due to low accuracy of the classifier, this would yield large errors. To improve the quality of predictions, one can employ the techniques, which make use of the available statistics of the events.

One of such techniques employs the confusion matrix and goes as follows. Let y_i be the averaged (over events) predictions of the classifier for all samples of i -th class (particle type). Then the confusion matrix C is defined by the following equation:

$$y_i = C\hat{y}_i, \quad \forall i. \quad (2.1)$$

where \hat{y}_i are the correct predictions (all zeros except for 1 at i -th position). Usually, and as we do in the paper, the confusion matrix is evaluated using the validation data set. Then, given an ensemble of events of interest, one can improve the averaged predictions of the classifier by multiplying them with C^{-1} .

As an enhancement to the described method, instead of employing the confusion matrix we suggest using a new neural network for improving averaged predictions of the classifier. This yields two benefits. First, the transformation of the averaged predictions becomes non-linear, hence allowing for more precise mappings. Second, the neural network can take into account not only the averaged predictions, but higher-order moments of the distribution

as well. This allows to improve the predictions by utilizing more information. Below we refer to this additional neural network as *the converter*.

The converter's architecture consists of 3 hidden fully-connected dense layers, having 32, 16, and 8 units respectively, with PReLU activation function [43]. The last layer is a dense layer with 4 units and softmax activation function. We observed that introducing more layers or increasing the number of units in the network does not improve the performance.

For training the converter, we made 10 000 ensembles of events, consisting of 5 000 samples each. To sample them, we first choose at random the fractions of four primary particles in an ensemble, and then randomly sample events for each of the particles. Our training and validation sets consist of 8 000 and 2 000 ensembles respectively. As we have a limited number of events, we allow ensembles to have non-empty intersections. It was verified that this does not lead to overfitting.

All of the ensembles were passed through the classifier. For a given ensemble, this yields 5000×4 predictions, corresponding to the classifier confidence on what was the primary particle in each of the events. By averaging over the events we get 4 numbers — the classifier prediction of the fractions of the elements in the ensemble. We also obtain the standard deviations of the predictions among the events, representing the diversity of the events in the ensemble. Together, these 8 numbers were given to the converter, which was trained to yield the true fractions of elements in the ensemble. It was observed that employing higher order moments of the distribution does not improve converter's performance.

Typical results of applying the chain of two neural networks for estimating the fractions of elements in an ensemble are depicted in figure 3. The averaged predictions of the classifier almost always indicate equal fractions of elements and thus are unreliable. The confusion matrix approach performs better, but sometimes yields significant reconstruction errors. Finally, the converter shows the best results. We also observed that the accuracy of the final predictions grows rapidly with the precision of the classifier. This is the reason why we have not dropped any blocks from the classifier architecture.

To estimate the error of the method, for each of the primary particles we evaluated the mean absolute error (MAE) between its true fraction in ensembles and the predicted one. For this purpose we used 2 000 ensembles from the validation set, the results are presented in table 2. As it can be expected, the method with the converter yields best performance. We estimate the absolute error of our method as 7% — the largest MAE between true and reconstructed fractions among elements.

An alternative metric that can be used for evaluating the performances of the methods is the maximum absolute error between true fractions and predicted ones. For the predictions obtained with the classifier, confusion matrix, and converter the corresponding errors are 0.6, 0.3, and 0.1 correspondingly. This shows that the converter yields best results.

If Monte-Carlo set includes all types of primary particles present in the data, the predictions of the converter can be directly interpreted as fractions of elements in an ensemble. In the opposite case one should use the prediction as weights for estimating the mean mass,

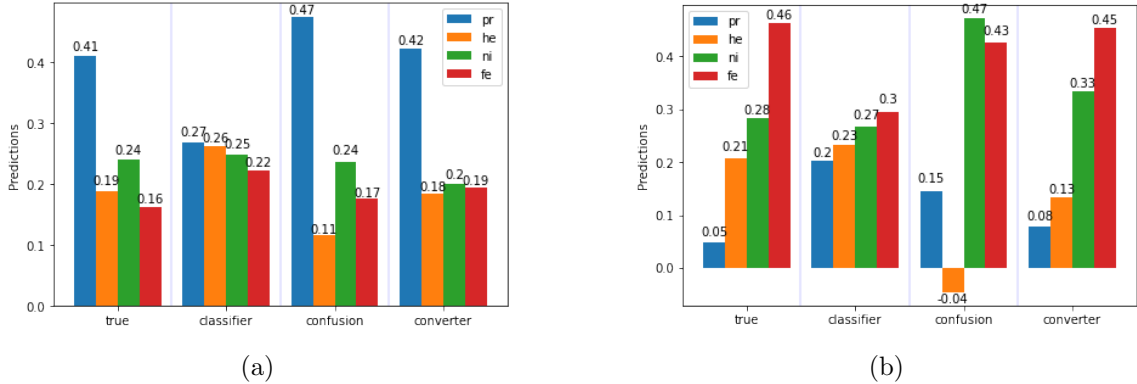


Figure 3. Results of predicting the ensemble composition for two different mixes. The fractions of elements are marked on the vertical axis. In each figure the four histograms, from left to right, correspond to 1) true fractions of elements, 2) averaged classifier predictions, 3) confusion matrix-corrected predictions, and 4) predictions of the converter.

	proton	helium	nitrogen	iron
classifier	0.10	0.11	0.11	0.09
confusion	0.06	0.14	0.12	0.04
converter	0.03	0.07	0.06	0.02

Table 2. MAE between true and reconstructed fractions of elements for different methods and particles.

m , of primary particles:

$$m = \sum_i p_i m_i , \quad (2.2)$$

where p_i and m_i are, respectively, the predictions and masses of the elements.

Errors for reconstructing the mass composition using the converter in other energy bins are summarized in table 3. Reconstruction accuracy of the method grows with the energy. This is due to the fact that the higher the energy of the primary particle is, the better is the quality of its footprint on the detectors. Correspondingly, the classifier, and hence the converter, can better distinguish different primary particles.

energy bin, log scale	18–18.25	18.25–18.5	18.5–18.75	18.75–19	> 19
averaged MAE	0.072	0.053	0.048	0.043	0.038

Table 3. MAE between true and reconstructed fractions of elements, averaged over the elements for different energy bins.

2.4 Model dependence

We examined the sensitivity of the method to the hadronic interaction model used for Monte-Carlo simulation in the following way. First, we trained the classifier and the

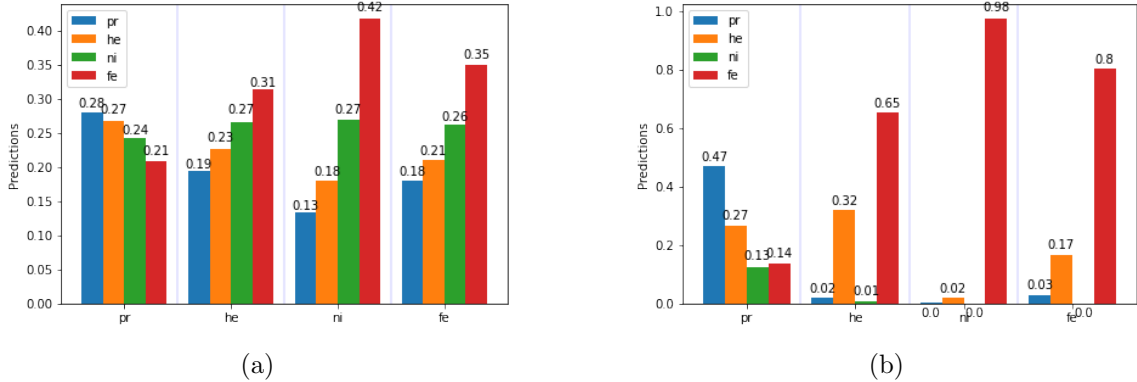


Figure 4. Predictions of the classifier and converter on the data simulated with QGSJET II-04 hadronic model. (a) — averaged predictions of the classifier, (b) — converter predictions. Four histograms on each of the panels, from left to right, show the predictions of fractions of elements in ensembles consisting only of protons, helium, nitrogen, and iron respectively.

converter on the data for QGSJET II-03 model only. Further, using the data simulated with QGSJET II-04 hadronic model, we made “pure” ensembles, consisting only of protons, helium, nitrogen, and iron respectively. These pure ensembles were analyzed by the classifier and then by the converter. The predictions are shown in figure 4.

From panels 4a and 4b one concludes that the classifier strongly overestimates masses of primary particles. This indicates a large systematic model error, which we estimate as the fraction of misclassified elements in table 4. Interestingly, the model error grows with the primary particle’s mass.⁴ Thus, by reaching high accuracy of predictions for individual events, our method reveals its sensitivity to the underlying hadronic model.

primary particle	proton	helium	nitrogen	iron	averaged
reconstruction error	0.53	0.68	1.00	0.20	0.60

Table 4. Systematic model error of the method, estimated as the fraction of misclassified elements.

There are two possible ways of overcoming the large model error problem. The first one is to identify a more reliable hadronic model by comparing some observable quantity in Monte-Carlo simulations and real data. In the ongoing researches in this direction one compares the simulated and measured profiles of extensive air showers [24, 28] or the recorded muon component of the signal [23, 27, 38].

The second way is to train the classifier on a Monte-Carlo simulated data for various hadronic models. Presumably, this will force the neural network to pick up only model-independent features, and thus reduce the model error.

We tried the second approach by combining Monte-Carlo simulated events for both QGSJET II-03 and QGSJET II-04 hadronic models. When the classifier was trained and tested on each of the models separately, it reached the accuracies 40.2% and 42.3% re-

⁴Predictions for the iron are an exception, since we do not have heavier elements in our training data.

spectively. Interestingly, this shows that QGSJET II-04 hadronic model produces more distinguishable events. The classifier trained and tested on the combined data yields 41.3% accuracy, which is close to the arithmetic mean of the models trained on each set of events separately. This indicates that model-independent training is possible, and to fully implement it one needs enough data simulated with more hadronic interaction models.

3 Conclusion

We have developed a method that allows one to achieve high accuracy in analyzing ensembles of events despite high variability of the data for individual events. The key idea of the method is to use a chain of two neural networks — one for analyzing individual events and one for analyzing the ensembles of events.

The method has been applied for identifying the mass composition of ultra-high-energy cosmic rays on the example of Monte-Carlo data for the Telescope Array Surface Detector. On this task, our approach yielded an unprecedented low error of 7% in reconstructing the fractions of 4 primary particles in ensembles of events. We have discussed the systematic error due to the choice of the hadronic interaction model and highlighted possible ways of how this error can be reduced.

Acknowledgments

The work is supported by the Ministry of Education of Russian Federation, grant number 075-15-2020-778.

A Regression approach

Instead of predicting types of primary particle for individual events, one may directly estimate their masses, i.e. consider the task as the regression problem. The benefit of choosing this approach is that, if it is precise enough, it would allow one to identify in an experimental data a primary particle that was not present in the Monte-Carlo set. Below we study this approach.

It is known that air shower parameters are most conveniently expressed as a function of the logarithm of the primary particle mass. Hence adopting the logarithm mass scale would make it easier for the neural network to learn the corresponding dependence. We employed this parametrization and labeled the particles with logarithms of their masses. For simplicity, the labels for protons, helium, nitrogen, and iron were approximated as 0, 1, 2, and 3 respectively (logarithm in base 4).

For training the network, we took the loss function to be the mean squared error, used Adam optimizer, and employed early stopping to avoid overfitting. Below we refer to this network as the *regressor*.

To study sensitivity of the network to nuclei not present in the data set, we trained two models. The first model was trained on all available data, while for the second we excluded all events with helium as a primary particle. The histograms illustrating the performances of the models are depicted in figure 5.

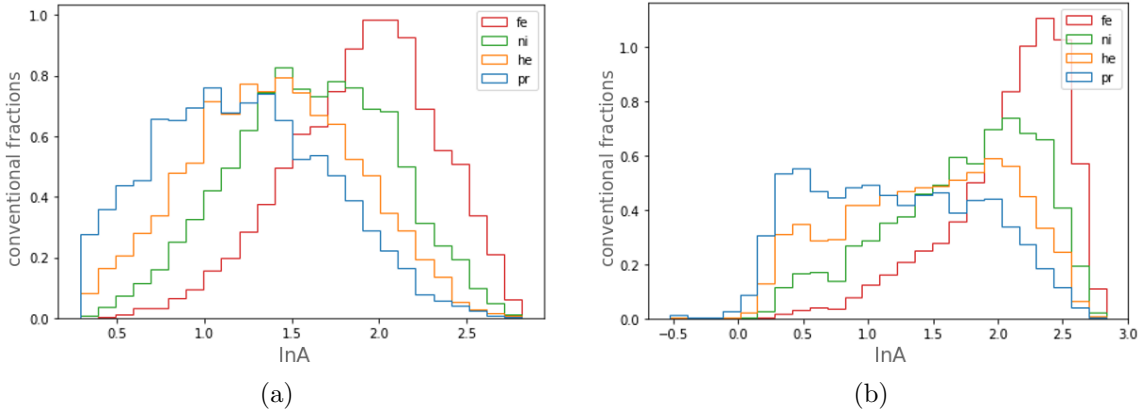


Figure 5. Histograms for predictions on the validation set. Case a) shows predictions for the neural network trained on all available primaries, while in case b) helium was excluded from the training data.

The figure shows that the regressor performs poorly on separating the elements. Namely, the histograms for different elements have large overlapping regions, and, for a given element, the averaged prediction of the logarithmic mass is far from its true value. Even for the model trained on all available data, the averaged predictions for protons, helium, nitrogen, and iron are 1.32, 1.40, 1.61, and 1.90 correspondingly. A positive observation is that the model that has never seen helium places it correctly somewhere between proton and nitrogen, with a similar shape of the distribution.

To obtain the mass composition, one can introduce the second neural network in a way, similar to how it was done in the classification regime. Namely, given an ensemble of events, one can obtain the distribution of the predictions of the regressor, similar to fig. 5. Further, this distribution can be splitted into n bins, thus forming a one-dimensional n -pixel “black and white” (as there is only one channel — value of the distribution at the given bin) image. The second neural network (the converter) in this case would be a convolutional network, analyzing this image and yielding true fractions of elements in the ensemble as the output.

We have tried this approach, with the predictions of the regressor splitted into 50 bins. It was observed, however, that this yields a larger error, approximately 0.5% bigger, than in the classification regime.

B Composition-sensitive parameters and cuts

The composition-sensitive parameters are obtained in a two-step procedure. At the first step a joint fit of the shower geometry and lateral distribution function (LDF) is performed using each detector’s trigger time and total signal. The shower front curvature parameter is determined at this fit. At the second step a number of additional parameters are estimated using time-resolved signals at each triggered detector. The details and corresponding references are given below.

The joint geometry and LDF fit has 7 free parameters:

- 1-2) Position of the shower core, $\vec{r}_{core} = (x_{core}, y_{core}, 0)$, defined in the coordinate system centered at the Central Laser Facility.
- 3-4) Arrival direction of the shower given by zenith and azimuthal angles, θ and ϕ .
- 5) Normalization of the shower's lateral distribution profile, S_{800} .
- 6) The time offset, t_0 .
- 7) Linsley front curvature parameter, a .

The target functions for the fit are

$$t(\vec{r}) = t_0 + t_{plane}(\vec{r}) + a \times LDF(r) \times \left(1 + \frac{r}{R_l}\right)^{1.5}, \quad (\text{B.1a})$$

$$S(r) = S_{800} \times LDF(r), \quad (\text{B.1b})$$

where r is the distance from the detector to the shower core (the shortest distance between a point and a line), $t_{plane}(\vec{r})$ is the arrival time of the shower plane to the detector located at \vec{r} , and $LDF(r)$ is the empirical lateral distribution profile, introduced in AGASA experiment [44] and then modified for TA data [13]:

$$t_{plane}(\vec{r}) = \frac{1}{c} \times (\vec{n}, (\vec{r} - \vec{r}_{core})), \quad (\text{B.2a})$$

$$LDF(r) = f(r)/f(800m), \quad (\text{B.2b})$$

$$f(r) = \left(\frac{r}{R_m}\right)^{-1.2} \left(1 + \frac{r}{R_m}\right)^{-(\eta-1.2)} \left(1 + \frac{r^2}{R_1^2}\right)^{-0.5}. \quad (\text{B.2c})$$

Here c is the speed of light, $\vec{n} = \vec{n}(\theta, \phi)$ is the unit vector along the direction of the shower axis, (\cdot, \cdot) stands for the scalar product, and

$$R_m = 90 \text{ m}, \quad R_1 = 1000 \text{ m}, \quad R_L = 30 \text{ m}, \quad (\text{B.3a})$$

$$\eta = 3.97 - 1.79(\sec(\theta) - 1). \quad (\text{B.3b})$$

The energy of the primary particle is estimated as a function of S_{800} and θ with the lookup table obtained from the Monte-Carlo simulations [13, 45].

Below is the complete list of the 23 composition-sensitive parameters used in the present paper. These parameters generally resemble ones from [36].

- 1-3) Reconstructed Linsley front curvature parameter (a), zenith angle (θ), and signal density at 800 m from the shower core (S_{800}), as described above.
- 4-5) χ^2 and *d.o.f.* for the joint geometry and LDF fit.
- 6-7) Area-over-peak of the signal at 1200 m and the corresponding slope parameter [46].
- 8) Number of triggered detectors.

9-10) Number of detectors that were used and excluded⁵ from the geometry fit [13].

11-15) $S_b \equiv \sum_i \left(S_i \times \left(\frac{r_i}{r_0} \right)^b \right)$ for five values of b : 2.5, 3.0, 3.5, 4.0, and 4.5. Here S_i and r_i are, respectively, the integral signal of i -th detector and its distance to the shower core, and $r_0 = 1200$ m [47].

- 16) The sum of integral signals from all of the detectors.
- 17) Asymmetry of the signal at the upper and lower layers of detectors [36].
- 18) Total number of peaks within all detectors [36].
- 19) Number of peaks for the detector with the largest signal.
- 20-21) Number of peaks present in the upper layer and not in the lower, and vice versa.
- 22) Minimal distance between the reconstructed air shower core and detectors array edge.
- 23) Number of detectors with signal longer than 128 time bins.

We have examined the usefulness of these parameters by training a neural network with two hidden fully-connected (dense) layers. The input of the network was one of the composition-sensitive parameters, and the output — the predicted type of the particle. The resulting ranking is as follows (random guessing corresponds to 25% accuracy):

- $\sim 30\%$ accuracy: Linsley front curvature.
- 27%–29% accuracy: total number of triggered detectors, number of detectors used for the geometry fit, reconstructed zenith angle, *d.o.f.*, AOP slope, $S_{4.5}$, and total number of peaks.
- $\sim 26\%$ accuracy: S_{800} , χ^2 , $S_{3.0}$, $S_{3.5}$, $S_{4.0}$, number of detectors excluded from the geometry fit, asymmetry of the signal in the upper and lower detectors, and total number of peaks present in the upper detector's layer and not in the lower.
- less than 26% accuracy: all others.

To ensure good quality of the events the neural network is trained on, we impose the following quality cuts:

- At least 7 detectors were triggered.
- Zenith angle is below 45° .
- The distance between the reconstructed air shower core and detectors array edge is more than 1200 m.

⁵Some of the detectors may be triggered by particles unrelated to the air shower. They are identified and excluded from the fit by the fitting procedure.

- $\chi^2/d.o.f.$ is less than 4 for separate geometry and the LDF fits, and is less than 5 for their joint fit.
- The error of estimating the arrival direction is less than 5° .
- The error of estimating S_{800} is less than 25%.

References

- [1] K.-H. Kampert and M. Unger, *Measurements of the cosmic ray composition with air shower experiments*, *Astroparticle Physics* **35** (2012) 660–678.
- [2] TELESCOPE ARRAY collaboration, R. U. Abbasi et al., *Constraints on the diffuse photon flux with energies above 10^{18} eV using the surface detector of the Telescope Array experiment*, *Astropart. Phys.* **110** (2019) 8–14, [[1811.03920](#)].
- [3] PIERRE AUGER collaboration, A. Aab et al., *Search for photons with energies above 10^{18} eV using the hybrid detector of the Pierre Auger Observatory*, *JCAP* **04** (2017) 009, [[1612.01517](#)].
- [4] PIERRE AUGER collaboration, A. Aab et al., *Probing the origin of ultra-high-energy cosmic rays with neutrinos in the EeV energy range using the Pierre Auger Observatory*, *JCAP* **10** (2019) 022, [[1906.07422](#)].
- [5] TELESCOPE ARRAY collaboration, R. U. Abbasi et al., *Search for Ultra-High-Energy Neutrinos with the Telescope Array Surface Detector*, *J. Exp. Theor. Phys.* **131** (2020) 255–264, [[1905.03738](#)].
- [6] D. Allard, E. Parizot and A. V. Olinto, *On the transition from galactic to extragalactic cosmic-rays: spectral and composition features from two opposite scenarios*, *Astropart. Phys.* **27** (2007) 61–75, [[astro-ph/0512345](#)].
- [7] R. Aloisio, V. Berezinsky, P. Blasi and S. Ostapchenko, *Signatures of the transition from Galactic to extragalactic cosmic rays*, *Phys. Rev. D* **77** (2008) 025007, [[0706.2834](#)].
- [8] G. T. Zatsepin and V. A. Kuzmin, *Upper limit of the spectrum of cosmic rays*, *JETP Lett.* **4** (1966) 78–80.
- [9] K. Greisen, *End to the cosmic-ray spectrum?*, *Physical Review Letters* **16** (1966) 748.
- [10] R. Aloisio, V. Berezinsky and A. Gazizov, *Ultra High Energy Cosmic Rays: The disappointing model*, *Astropart. Phys.* **34** (2011) 620–626, [[0907.5194](#)].
- [11] HiRES collaboration, R. U. Abbasi et al., *First observation of the Greisen-Zatsepin-Kuzmin suppression*, *Phys. Rev. Lett.* **100** (2008) 101101, [[astro-ph/0703099](#)].
- [12] PIERRE AUGER collaboration, J. Abraham et al., *Observation of the suppression of the flux of cosmic rays above 4×10^{19} eV*, *Phys. Rev. Lett.* **101** (2008) 061101, [[0806.4302](#)].
- [13] TELESCOPE ARRAY collaboration, T. Abu-Zayyad et al., *The Cosmic Ray Energy Spectrum Observed with the Surface Detector of the Telescope Array Experiment*, *Astrophys. J. Lett.* **768** (2013) L1, [[1205.5067](#)].
- [14] M. S. Pshirkov, P. G. Tinyakov and F. R. Urban, *Mapping UHECRs deflections through the turbulent galactic magnetic field with the latest RM data*, *Mon. Not. Roy. Astron. Soc.* **436** (2013) 2326, [[1304.3217](#)].

[15] PIERRE AUGER collaboration, A. Aab et al., *Depth of maximum of air-shower profiles at the Pierre Auger Observatory. II. Composition implications*, *Phys. Rev. D* **90** (2014) 122006, [[1409.5083](#)].

[16] R. U. Abbasi et al., *Study of Ultra-High Energy Cosmic Ray composition using Telescope Array’s Middle Drum detector and surface array in hybrid mode*, *Astropart. Phys.* **64** (2015) 49–62, [[1408.1726](#)].

[17] TELESCOPE ARRAY collaboration, R. U. Abbasi et al., *Depth of Ultra High Energy Cosmic Ray Induced Air Shower Maxima Measured by the Telescope Array Black Rock and Long Ridge FADC Fluorescence Detectors and Surface Array in Hybrid Mode*, *Astrophys. J.* **858** (2018) 76, [[1801.09784](#)].

[18] HiRES collaboration, R. U. Abbasi et al., *Indications of Proton-Dominated Cosmic Ray Composition above 1.6 EeV*, *Phys. Rev. Lett.* **104** (2010) 161101, [[0910.4184](#)].

[19] TELESCOPE ARRAY collaboration, R. U. Abbasi et al., *Mass composition of ultrahigh-energy cosmic rays with the Telescope Array Surface Detector data*, *Phys. Rev. D* **99** (2019) 022002, [[1808.03680](#)].

[20] PIERRE AUGER collaboration, A. Aab et al., *Deep-learning based reconstruction of the shower maximum X_{max} using the water-Cherenkov detectors of the Pierre Auger Observatory*, *JINST* **16** (2021) P07019, [[2101.02946](#)].

[21] PIERRE AUGER collaboration, A. Aab et al., *Combined fit of spectrum and composition data as measured by the Pierre Auger Observatory*, *JCAP* **04** (2017) 038, [[1612.07155](#)].

[22] M. Y. Kuznetsov and P. G. Tinyakov, *UHECR mass composition at highest energies from anisotropy of their arrival directions*, *JCAP* **04** (2021) 065, [[2011.11590](#)].

[23] R. Abbasi, M. Abe, T. Abu-Zayyad, M. Allen, R. Azuma, E. Barcikowski et al., *Study of muons from ultrahigh energy cosmic ray air showers measured with the telescope array experiment*, *Physical Review D* **98** (2018) 022002.

[24] A. Aab, P. Abreu, M. Aglietta, E. Ahn, I. Al Samarai, I. Albuquerque et al., *Testing hadronic interactions at ultrahigh energies with air showers measured by the pierre auger observatory*, *Physical review letters* **117** (2016) 192001.

[25] T. Abu-Zayyad, K. Belov, D. Bird, J. Boyer, Z. Cao, M. Catanese et al., *Evidence for changing of cosmic ray composition between 10 17 and 10 18 ev from multicomponent measurements*, *Physical Review Letters* **84** (2000) 4276.

[26] A. V. Glushkov, I. T. Makarov, M. I. Pravdin, I. E. Sleptsov, D. S. Gorbunov, G. I. Rubtsov et al., *Muon content of ultrahigh-energy air showers: Yakutsk data versus simulations*, *JETP Letters* **87** (2008) 190–194.

[27] L. Dedenko, A. Lukyashin, T. Roganova and G. Fedorova, *Testing of the epos lhc, qgsjet01, qgsjetii-03 and qgsjetii-04 hadronic interaction models via help of the atmospheric vertical muon spectra*, in *Journal of Physics: Conference Series*, vol. 934, p. 012017, IOP Publishing, 2017.

[28] W. Apel, J. Arteaga-Velázquez, K. Bekk, M. Bertaina, J. Blümer, H. Bozdog et al., *Probing the evolution of the eas muon content in the atmosphere with kascade-grande*, *Astroparticle Physics* **95** (2017) 25–43.

[29] Y. A. Fomin, N. Kalmykov, I. Karpikov, G. Kulikov, M. Y. Kuznetsov, G. Rubtsov et al., *No*

muon excess in extensive air showers at 100–500 pev primary energy: Eas-msu results, *Astroparticle Physics* **92** (2017) 1–6.

- [30] J. G. Gonzalez, *Measuring the muon content of air showers with icetop*, in *Epj web of conferences*, vol. 99, p. 06002, EDP Sciences, 2015.
- [31] A. Alekseev, E. Atlasov, N. Bolotnikov, A. Bosikov, N. Dyachkovskiy, N. Gerasimova et al., *Status of the yakutsk air shower array and future plans*, *arXiv preprint arXiv:2107.07528* (2021) .
- [32] H. Dembinski, J. Arteaga-Velázquez, L. Cazon, R. Conceição, J. Gonzalez, Y. Itow et al., *Report on tests and measurements of hadronic interaction properties with air showers*, in *EPJ Web of Conferences*, vol. 210, p. 02004, EDP Sciences, 2019.
- [33] T. Abu-Zayyad, R. Aida, M. Allen, R. Anderson, R. Azuma, E. Barcikowski et al., *The surface detector array of the telescope array experiment*, *Nuclear Instruments and Methods in Physics Research Section A: Accelerators, Spectrometers, Detectors and Associated Equipment* **689** (2012) 87–97.
- [34] D. Heck, J. Knapp, J. Capdevielle, G. Schatz, T. Thouw et al., *Corsika: A monte carlo code to simulate extensive air showers*, *Report fzka* **6019** (1998) .
- [35] S. Ostapchenko, *Qgsjet-ii: towards reliable description of very high energy hadronic interactions*, *Nuclear Physics B-Proceedings Supplements* **151** (2006) 143–146.
- [36] R. Abbasi, M. Abe, T. Abu-Zayyad, M. Allen, R. Azuma, E. Barcikowski et al., *Mass composition of ultrahigh-energy cosmic rays with the telescope array surface detector data*, *Physical Review D* **99** (2019) 022002.
- [37] D. Ivanov, O. Kalashev, M. Y. Kuznetsov, G. Rubtsov, T. Sako, Y. Tsunesada et al., *Using deep learning to enhance event geometry reconstruction for the telescope array surface detector*, *Machine Learning: Science and Technology* **2** (2020) 015006.
- [38] PIERRE AUGER collaboration, A. Aab et al., *Extraction of the muon signals recorded with the surface detector of the Pierre Auger Observatory using recurrent neural networks*, *JINST* **16** (2021) P07016, [[2103.11983](https://arxiv.org/abs/2103.11983)].
- [39] M. Abadi, P. Barham, J. Chen, Z. Chen, A. Davis, J. Dean et al., *Tensorflow: A system for large-scale machine learning*, in *12th {USENIX} symposium on operating systems design and implementation ({OSDI} 16)*, pp. 265–283, 2016.
- [40] T. O’Malley, E. Bursztein, J. Long, F. Chollet, H. Jin, L. Invernizzi et al., “Kerastuner.” <https://github.com/keras-team/keras-tuner>, 2019.
- [41] D. P. Kingma and J. Ba, *Adam: A method for stochastic optimization*, *arXiv preprint arXiv:1412.6980* (2014) .
- [42] S. J. Reddi, S. Kale and S. Kumar, *On the convergence of adam and beyond*, *arXiv preprint arXiv:1904.09237* (2019) .
- [43] K. He, X. Zhang, S. Ren and J. Sun, *Delving deep into rectifiers: Surpassing human-level performance on imagenet classification*, in *Proceedings of the IEEE international conference on computer vision*, pp. 1026–1034, 2015.
- [44] T. Teshima, Y. Matsubara, T. Hara, N. Hayashida, M. Honda, F. Ishikawa et al., *Properties of 109-1010 gev extensive air showers at core distances between 100 and 3000 m*, *Journal of Physics G: Nuclear Physics* **12** (1986) 1097.

- [45] Telescope Array Collaboration, *CORSIKA Simulation of the Telescope Array Surface Detector*, *arXiv e-prints* (Mar., 2014) arXiv:1403.0644, [[1403.0644](#)].
- [46] J. Abraham, P. Abreu, M. Aglietta, C. Aguirre, D. Allard, I. Allekotte et al., *Upper limit on the diffuse flux of ultrahigh energy tau neutrinos from the pierre auger observatory*, *Physical Review Letters* **100** (2008) 211101.
- [47] G. Ros, A. D. Supanitsky, G. A. Medina-Tanco, L. del Peral, J. C. D'Olivo, M. D. Rodriguez-Frias et al., *A new composition-sensitive parameter for Ultra-High Energy Cosmic Rays*, *Astropart. Phys.* **35** (2011) 140–151, [[1104.3399](#)].